# Precision Pointing Compensation for DSN Antennas With Optical Distance Measuring Sensors

R. E. Scheid
Guidance and Control Section

*The pointing control loops of DSN antennas do not account for unmodeled deflections of the primary and secondary reflectors. As a result, structural distortions due to unpredictable environmental loads can result in uncompensated boresight shifts which degrade pointing accuracy.*

*The design proposed here can provide real-time bias commands to the pointing control system to compensate for environmental effects on pointing performance. The bias commands can be computed in real time from optically measured deflections at a number of points on the primary and secondary reflectors. Computer simulations with a reduced-order finite-element model of a DSN antenna validate the concept and lead to a proposed design by which a ten-to-one reduction in pointing uncertainty can be achieved under nominal uncertainty conditions.*

## I. Introduction

Current pointing system designs for DSN antennas do not incorporate effects beyond some reference plane which separates the control system from the antenna tipping structure, which includes the primary reflector, the secondary reflector, the quadripod, and the feedcone. For example, the DSN 70-meter antenna pointing system determines the main az-el pointing servo-drive error signals from a two-axis autocollimator mounted on the Intermediate Reference Structure (IRS) (see Fig. 1) [1]. By projecting a light beam onto a precision mirror mounted on the Master Equatorial (ME) and measuring the angular deviation of the reflected beam from the nominal orientation, the autocollimator determines an error signal which results from the nonparallelism of the two surfaces.

Because the tipping structure is outside the pointing control loop, uncompensated boresight shifts will typically result from the distortion of the structure due to environmental loads. Self-compensating effects in the structural design of the antenna limit the net peak pointing offset to approximately 100 millidegrees even though structural deformations of the components of the antenna system can individually produce equivalent pointing shifts of nearly 1 degree due to unmodeled environmental loads.

The schematic diagram in Fig. 2 illustrates the effect of structural distortion on pointing capability. According to design specifications, the axes of the main reflector paraboloid and the subreflector hyperboloid lie on an axis normal to the IRS, which passes through the vertex of the paraboloid. As indi-

cated by the broken line, environmental forces which distort the structure prevent rays reflected from different segments of the antenna from being focused onto the IRS reference axis. The design objective of a pointing error compensation system is to bias the pointing command so that the centroid of energy with respect to the target falls along the IRS reference axis. Other DSN antennas also employ compensator designs which do not correct for the effect of distortions due to unmodeled environmental loads on the tipping structure.

The principal environmental factors acting on the antenna are gravity, wind, and thermal effects. Gravity, the largest but most predictable load on the structure, causes sagging in the primary reflector and varies as a function of elevation angle. In addition, the gravitational effects lead to a displacement of the quadripod structure and a resultant displacement of the subreflector. The effects of gravity can be modeled by means of the finite element models which are available for DSN antennas, and, since the effects are predictable, the resulting boresight errors can be offset through a calibration process. The resulting look-up tables then provide an elevation pointing command bias signal to compensate for gravitationally induced pointing errors as a function of elevation angle. Wind and thermal effects on the structure lead to considerably less severe distortions but are also much less predictable.

By using look-up tables to bias the elevation pointing command to compensate for gravitational effects, a blind pointing capability of approximately 10 millidegrees is currently achievable in weather conditions that range from benign to moderately windy. With the recently completed upgrades to enlarge and improve the shape of the large DSN tracking antennas in combination with future plans to quadruple the upper operating frequency, it is desirable to improve pointing precision to 1 millidegree so as to fully realize the benefits of the upgrades for 32-GHz (Ka-band) operation.

The following presents a description and analysis of a real-time optical measurement and processing concept which delivers real-time pointing system bias commands to compensate for the effects of environmentally induced structural distortions. The concept requires optical measurements of the displacements of selected points on the primary and secondary reflectors relative to some reference coordinate system which lies at the base of the feedcone (e.g., the pointing reference plane in Fig. 2).

The Spatial High-Accuracy Position Encoding Sensor (SHAPES) system under development at JPL [2] was taken as the baseline sensor for the measurement system since it is capable of delivering multiple simultaneous high-speed (10 frames per second) ranging measurements with accuracies at the submillimeter level. SHAPES is a time-of-flight laser ranging sensor which measures ranges from multiple sources to retroreflector targets placed at optically unobstructed locations. By means of a system of fiber-optic connections, each SHAPES sensor head can accommodate up to 24 targets, whose actual locations can be physically remote from the head. By means of triangulation, the range measurements taken from sensor heads fixed with respect to a known reference coordinate system can be combined to give two- and three-dimensional displacement coordinates for a given retroreflector. A discussion of the effects on the SHAPES system due to anticipated environmental uncertainties in DSN applications can be found in [3].

The discussion here deals only with the effects of unmodeled structural distortions beyond the reference coordinate plane (i.e., primary reflector, secondary reflector, quadripod, and feedcone) and assumes an a priori spatial knowledge of a reference coordinate system, the determination of which is a subject of current investigations in this technology. While others have approached the problem of real-time compensation by combining SHAPES technology with purely geometrical analysis [4], the treatment here is based on the solution of an underlying structural estimation problem combined with a geometrical synthesis. It is the framework of the estimation problem that provides for a meaningful quantitative evaluation of a given compensator design.

Section II begins with a general description of the proposed compensator design and continues with a more detailed discussion of the resulting structural and geometrical problems. Section III presents the simulation results based on a reduced-order finite-element model of a DSN antenna. Section IV outlines the conclusions of this work.

## II. Problem Formulation

### A. Compensator Design

The current compensator design is based on a calibration process for the effects of external loads such as gravity which can be predicted by finite-element (FE) modeling analysis (Fig. 3). The result is a tabulation of compensation signals which depends on the current attitude of the antenna tipping structure.

As a starting point for the calibration process, the modeled external forces are taken as static load inputs to a high-order finite-element model, and this results in a predicted estimate for the shape of the main reflector as well as location estimates for the subreflector and the feed. From this a parabolic fit routine is used to obtain a least-squares fit of the main reflector to a parabola of revolution. The effective boresight axis can then be determined as a linear combination of terms

which depends on the parameters of the best-fit parabola and the position of the other rigidly modeled structural components of the system [5]. More precisely, the boresight error is determined as a linear combination of the vertex shift and the rotation of the best-fit parabola, the lateral translation and rotation of the subreflector, and the lateral translation of the feed.

Such a control process is called open-loop in that there is no feedback from the state of the system. The development proposed here is a real-time structural-optical compensator (Fig. 4) which incorporates measurement data into the process of estimating the state of the structural system. The blocks of the design which indicate the parabolic best fit and the boresight determination can be used as before. The crucial block of this real-time compensator design is the structural-optical estimator which combines modeled responses to static loads with real-time measurement data (Fig. 5).

This block has the structure of a predictor-corrector system whereby the difference between the observed data and what can be predicted by a priori modeling leads to a correction which is added to the prediction derived before measurements are taken. Thus the dashed box in Fig. 5 denotes the structural predictor leading to the estimate which conceptually determines the current structural compensator (Fig. 4). The key ingredient in the structural-optical estimator is the filter gain which is determined by the solution to an optimization problem posed in the finite-element space.

In the next subsections, key components of the structural-optical compensator design are discussed in more detail. The structural-optical estimator is derived by means of a shape-determination problem posed in a finite-element space. Next the parabolic fit analysis is discussed and specialized to the two-dimensional case, which was the version used in the simulations subsequently undertaken.

## B. Static Shape Determination

A number of important emerging applications in the technology of large space structures can be appropriately analyzed as statically loaded structural systems. This approach is applicable to systems where the time-dependent effects are negligible and where the relevant forces do not significantly excite dynamic behavior in the system. More generally, one can consider problem settings where the stiffness properties dominate the mass properties in determining the energy balances. Then a static response of the structure defines a reference configuration about which motions can be resolved with greater accuracy. In this context one can include applications where the time-varying effects of the model are changing slowly with respect to the scale on which operations must be carried out. These quasi-static disturbances may, for example, include gravitational and thermal effects.

The introduction of statistical model errors allows the smearing of effects which have been ignored in the modeling or which occur on too fine a scale to be adequately modeled. This treatment of the system error distinguishes this approach from purely dynamic treatments of the problem. As a result the observational data can be statistically referenced to a plant, and questions regarding the validity of the estimates can be treated in a statistical framework which includes modeling errors as well as observational errors. The approach developed here leads to a framework which is suitable for combining a variety of geometric and structural models with a variety of mechanical and electro-optical sensing systems.

Of particular interest are the many large space antenna systems such as the DSN antennas. Performance requirements in communications and radiometry call for antennas with increasingly large diameters and surface-error requirements far beyond current capabilities.

This section summarizes the basic analysis which supports the static shape determination algorithms. This approach to shape estimation is part of an integrated methodology combining the techniques of modeling, identification, and estimation for static control of distributed systems. A more complete discussion of this framework is given in [6] and [7].

Let the state variable be given by $\vec{u}$. The models considered have the general form

$$A\vec{u} = C\vec{f} + B\vec{\omega} \tag{1}$$

$$\vec{y} = H\vec{u} + F\vec{\eta} \tag{2}$$

Here $A$ is an operator representing the system model. The preliminary analysis can begin with coarse geometric models which are suitable for resolving overall features. More detailed resolutions are then obtained by taking $A$ to be a stiffness matrix. This type of fine-scale resolution can be idealized by taking $A$ to be an invertible self-adjoint elliptic differential operator defined over some spatial domain. The operator $A$ is assumed to be invertible with inverse $\Phi$; this gives

$$\Phi A = I$$

where $I$ is the identity. The two terms on the right-hand side of Eq. (1) respectively represent the modeled and unmodeled loads on the system. In particular $C$ is an operator that characterizes the relevant deterministic forces, while $B$ is an operator that characterizes the process errors that influence the state.

The vector $\vec{y}$ represents an observation of the system (i.e., a set of measurements). $H$ is an operator that characterizes the state-to-observation map. It is assumed that the observation space has dimension $N_s$ which corresponds to a finite-dimensional sensing scheme. The second term on the right-hand side of Eq. (2) represents the measurement errors present in the observation $\vec{y}$. The integrated form of the observation equation is given by

$$\vec{y} = H\Phi C\vec{f} + H\Phi B\vec{\omega} + F\vec{\eta}$$

There are three inner-product spaces of primary interest: the input space $S_1$ to which the process error $B\vec{\omega}$ and the deterministic input $C\vec{f}$ belong; the state space $S_2$ containing the state $\vec{u}$; and the measurement space $S_3$ where the data $\vec{y}$ and the observation error $F\vec{\eta}$ belong. The inner product between two arbitrary elements $u$ and $v$ in the space $S_i$ is denoted by $\langle u,v \rangle_i$ or by the simpler notation $u * v = \langle u,v \rangle_i$. Similarly, $uv*$ denotes an outer product. The corresponding norms are given by $\| \cdot \|_i$ or, when the context is clear, by the simpler notation $\| \cdot \|$.

The appropriately dimensioned operators $B$ and $F$ model the statistical influence of the process error and the measurement error; these errors, $\omega$ and $\eta$, form the model error vector

$$\xi = (\omega, \eta)$$

which represents spatial white noise and is characterized by the covariance operator

$$E(\xi\, \xi^*) = I$$

where $E(\cdot)$ denotes the expectation operator. More precisely, for $x_1 \epsilon S_1$ and $x_3 \epsilon S_3$, one has

$$E[\vec{\omega}] = 0 \qquad E[\langle \vec{x}_1, \vec{\omega} \rangle_1 \vec{\omega}] = \vec{x}_1$$

$$E[\vec{\eta}] = 0 \qquad E[\langle \vec{x}_3, \vec{\eta} \rangle_3 \vec{\eta}] = \vec{x}_3$$

The limiting cases $\| B \| \to 0$ and $\| F \| \to 0$ respectively represent the assumptions of perfect modeling and perfect measurements.

The abstract quantities in Eqs. (1) and (2) take on relevant physical meanings in the context of the application under consideration. Here the state $\vec{u}$ represents the elastic deformation of the antenna tipping structure as modeled by $A$, a finite-element stiffness matrix. The modeled forces $C\vec{f}$ are restricted to gravity only while the process-error term $B\vec{\omega}$ represents all unmodeled environmental loads as well as inaccuracies in the finite-element model. The vector of observations $\vec{y}$ results from the sampling of the state by the measurement system (i.e., SHAPES), which is characterized by the state-to-observation map $H$ and the measurement error term $F\vec{\eta}$.

The preceding assumptions lead to an appropriate framework for the analysis of minimum variance estimators of the state. Here the expected observation $\vec{m}$ is characterized by

$$\vec{m} = H\Phi C\vec{f}$$

$$E[\vec{y}] = \vec{m} \qquad E[(\vec{y} - \vec{m})(\vec{y} - \vec{m})^*] = HR_\omega H^* + R_\eta$$

and the expected process and measurement covariances $R_\omega$ and $R_\eta$

$$R_\omega = \Phi BB^*\Phi^* \qquad R_\eta = FF^* \tag{3}$$

The resulting formulas are similar to the typical Kalman gain formulations used in the analysis of dynamical systems [8]. The minimum-variance estimate $u_{est}$ has the form

$$\vec{u}_{est} = \vec{u}_o + g(\vec{y} - \vec{m})$$

$$\vec{u}_o = C\vec{f}$$

where the gain $g$ is given by

$$g = R_\omega H^* (R_\eta + HR_\omega H^*)^{-1}$$

Thus, as illustrated in Fig. 5, the structural-optical estimator acts as a predictor-corrector scheme where the prediction comes from the modeled value of the state and where the correction is determined by the discrepancy between the modeled state and the actual measurements.

The covariance operator associated with the estimation error is given by

$$P = R_\omega - R_\omega H^* (R_\eta + HR_\omega H^*)^{-1} HR_\omega \tag{4}$$

The covariance then can be used to determine the expected error before and after measurements:

$$E[\| u - u_o \|^2] = tr[R_w]$$

$$E[\| \vec{u} - \vec{u}_{est} \|^2] = tr[P] \tag{5}$$

From Eqs. (3), (4), and (5) it follows that

$$E\left[\|\vec{u}-\vec{u}_{est}\|^2\right] < E\left[\|\vec{u}-\vec{u}_{o}\|^2\right]$$

That is, the incorporation of measurements reduces the expected error in the estimate of the state (i.e., the shape of the antenna tipping structure).

In the case where $A$ represents a finite-element stiffness matrix, a number of static loading problems must be solved in order to approximate the gain and the covariance. For example, when the state-to-observation map $H$ returns point-values of the state, one needs to compute fundamental solutions which correspond to unit static loads at the observed points.

One can also consider possibilities for recursive batch processing of data sets obtained by means of different sensing strategies. For example, Eq. (2) can be replaced by two sets of observations:

$$\vec{y}_1 = H_1\vec{u} + F_1\vec{\eta}_1$$

$$\vec{y}_2 = \vec{H}_2\vec{u} + \vec{F}_2\vec{\eta}_2$$

An analysis of the second-order statistics of the related estimation error can also be conducted. Such an approach was implemented in [9] to combine optical measurements with data taken from radiation patterns to obtain optimal estimates for antenna surface deformations.

## C. Parabolic Fit Analysis

The problem of fitting a reflector deformation model with many degrees of freedom to a parabola of revolution has been treated for DSN applications elsewhere in detail (see, for example, [10], [11]). The problem is generally treated in a least-squares formulation about the undisturbed dish, and the minimization is carried out with respect to the sums of squares of the pathlength errors associated with each point in the discretization. It can be shown that the pathlength error at a point can be trigonometrically related to the normal component of the surface error (cf. Eq. (7)). Here is a summary of the analysis when specialized to two spatial dimensions. The relevant equation is

$$z = \frac{y^2}{4f}$$

$$-1 \leqslant y \leqslant 1$$

where the coordinates $y$ and $z$ and the focal parameter $f$ have been normalized by the radius of the dish.

The grid $G = \{(y_i, z_i)\}$ is chosen so that the deformation can be represented sufficiently accurately by these point values. For this application the $y_i$-values are the nodal locations of the finite-element model, and the corresponding $z_i$-values are the displacements at the nodes. The differential distortion of the parabola is represented by the so-called homology parameters $\vec{h} = (h^{(1)}, h^{(2)}, h^{(3)}, h^{(4)})^T$ where

$h^{(1)}$ = shift in vertex ($y$-coordinate)

$h^{(2)}$ = shift in vertex ($z$-coordinate)

$h^{(3)}$ = rotation about origin in the $y/z$ plane

$h^{(4)}$ = relative change in focal length ($\Delta f/f$)

The analysis is very similar in the three-dimensional case, where there are two additional homology parameters (one for the shift in vertex, one for the rotation).

Retaining only first-order terms, one can compute the differential distortion at the point $\binom{y}{z}$:

$$\begin{pmatrix} h^{(1)} \\ h^{(2)} \end{pmatrix} + \begin{bmatrix} 1 & -h^{(3)} \\ h^{(3)} & 1 \end{bmatrix} \begin{pmatrix} y \\ z \end{pmatrix} + \begin{pmatrix} 0 \\ -zh^{(4)} \end{pmatrix}$$

where geometrically these three terms respectively represent the translation, rotation, and focal shift of the parabola. Thus the differential displacement of the parabolic point is given by

$$\hat{C}(y,z)\vec{h}$$

where the 2 X 4 matrix $\hat{C}(y,z)$ is defined by

$$\hat{C}(y,z) = \begin{pmatrix} 1 & 0 & -z & 0 \\ 0 & 1 & y & -z \end{pmatrix}$$

The normal to the surface at $\binom{y}{z}$ is given by

$$\vec{n}(y,z) = \frac{1}{\sqrt{\frac{z}{f}+1}} \begin{pmatrix} \frac{-y}{2f} \\ 1 \end{pmatrix}$$

Then projecting the deflection onto the normal gives

$$\hat{B}(y,z) = \vec{n}(y,z)^T\,\hat{C}(y,z) = \frac{1}{\sqrt{\frac{z}{f}+1}} \left(\frac{-y}{2f}, 1, \left(\frac{yz}{2f}+y\right), -z\right)$$

The deflection at each point is also projected onto the normal direction

$$\rho(y,z)\vec{n}(y,z)$$

where $\rho(y,z)$ is a scalar.

It is now possible to form the normal equations on the grid $G$ by defining the $N \times 4$ matrix

$$\hat{A} = \begin{bmatrix} \hat{B}(y_1,z_1) \\ \hat{B}(y_2,z_2) \\ \vdots \\ \hat{B}(y_N,z_N) \end{bmatrix}$$

and the $N$-dimensional vector

$$\vec{b} = \begin{pmatrix} \rho(y_1,z_1) \\ \vdots \\ \rho(y_N,z_N) \end{pmatrix}$$

This allows one to form the $N$-dimensional residual vector for the normal deflections

$$\vec{r} = \hat{A}\vec{h} - \vec{b}$$

The best-fit optimization problem is now posed as a minimization of the residual with respect to the norm

$$\|\vec{r}\|_W^2 = \vec{r}^T W \vec{r}$$

where $W$ is an $N \times N$ symmetric positive definite matrix (see, for example, [12]). The resulting normal equations are given by

$$(\hat{A}^T W \hat{A})\vec{h} = \hat{A}^T W \vec{b} \tag{6}$$

or equivalently

$$(\tilde{A}^T \tilde{A})\vec{h} = \tilde{A}^T \tilde{\vec{b}}$$

$$\tilde{A} = W^{\frac{1}{2}} \hat{A}$$

$$\tilde{\vec{b}} = W^{\frac{1}{2}} \vec{b}$$

$W$ can be chosen as a diagonal matrix

$$W = \text{diag}\,[w_1, w_2, \ldots, w_N]$$

where $w_i$ has the form

$$w_i = a_i \left( \frac{f}{f + z_i} \right) \tag{7}$$

Here $a_i$ is the length (or area) associated with each point. The additional factor results in a minimization with respect to path length.

The solution of Eq. (6) is then given by

$$\vec{h} = \hat{T}\vec{b}$$

$$\hat{T} = (\hat{A}^T W \hat{A})^{-1} \hat{A}^T W \tag{8}$$

Here the $4 \times N$ matrix $\hat{T}$ is often called the pseudo-inverse.

## III. Model Description and Simulation Results

The functional block diagram in Fig. 6 outlines the conceptual framework in which the boresight determination problem is treated in this article. The relevant synthesis problem focuses on the determination of three antenna boresights:

(1) A gravitational boresight derived from a model for gravitational deformations combined with a parabolic fit.

(2) A true boresight derived from a model for gravitational plus unmodeled deformations combined with a parabolic fit.

(3) An estimated boresight derived from an estimator which integrates structural finite-element models, gravitational deformation models, sampled measurements of the true deformation vector, and a parabolic fit.

As has been previously noted, current boresight pointing technology is based on a calibration with respect to forces whose effects can be adequately predicted (e.g., gravity). However, this calibration process is less successful when the disturbance forces cannot be adequately modeled (e.g., thermal effects, wind, etc.). The subsequent simulations were intended to determine the requirements for a boresight estimator which, under nominal uncertainty conditions, would recover the true boresight to within 1 millidegree, a requirement beyond the capabilities of the current calibration process. The design parameters included the properties of the disturbance forces (modeled and unmodeled) as well as the requirements for the sensing configuration (number, placement, and accuracy). In

order to make the simulations more tractable, simplifications were introduced in the structural, geometrical, and statistical analyses.

For the structural analysis a reduced two-dimensional antenna deformation model was derived from a high-order finite-element model of a 34-meter DSN antenna (DSS-15). More precisely, two ribs were designated as the north and south ribs, and all deformations calculated from the three-dimensional model were projected onto this pair (see Fig. 7). The total number of nodal values retained was 26, and these were evenly divided between the two ribs.

For the geometrical analysis of the parabolic fit, the two-dimensional least-squares formulation given in Section II.B was implemented. In addition, only the third component of the homology vector ($h^{(3)}$) was used in the estimate of the boresight. This component, the rotation about the origin in the $y/z$ plane, is the geometrical boresight of the best-fit parabola and corresponds to the largest term in the computation of the structural boresight [5]. Thus, in the spirit of the analysis of Section II.B this work focuses on the boresight errors associated with the structural deformations of the primary reflector, and attention is restricted to the dominant contribution. The other relevant components of the structural boresight noted in Section II.A (vertex shift of best-fit parabola, lateral translational and rotation of the subreflector, and lateral translation of the feed) could also have been included in the analysis, making the simulations somewhat more complex. Instead, the boresight errors associated with estimating these contributions were acceptably bounded. In particular, it was determined that the SHAPES system when combined with a charge-coupled device (CCD) angle-measuring camera is capable of measuring the subreflector position with sufficient accuracy so that the resulting uncertainty in the boresight is smaller than the errors considered here.

For the statistical analysis the weighting matrices for the process error and the measurement error were taken to be scalar:

$$F = \sigma_\eta I$$
$$B = \sigma_\omega I \tag{9}$$

where $I$ is the identity. More general forms for $F$ and $B$ could be used to characterize such features as a structural finite-element model which is less reliable at some nodes than at others, or a measurement system with some components that are more accurate than others.

The preceding assumptions lead to the following version of the formulations given in Section II:

$$A\vec{u} = C\vec{f} + \sigma_\omega \vec{\omega} \tag{10}$$

$$\vec{y} = H\vec{u} + \sigma_\eta \vec{\eta} \tag{11}$$

$$\beta = \hat{Q}\hat{T}\hat{N}\vec{u} \tag{12}$$

Here Eqs. (10) and (11) are simply Eqs. (1) and (2) combined with the simplification given by Eq. (9). In Eq. (12), $\hat{N}$ is the mapping that projects the state (i.e., the deflection of the structure) onto the normal component. Then $\hat{T}$ is the pseudo-inverse given in Eq. (8) which maps the normal deflections onto the vector of homology parameters $\vec{h}$. And finally, $\hat{Q}$ maps the homology parameters onto the boresight value. In accordance with the simplifying assumptions outlined here, $\hat{Q}$ is given by

$$\hat{Q} = [0,0,1,0]$$

That is, $\hat{Q}$ is a projection onto the third homology parameter ($h^{(3)}$), which denotes the rotation about the origin in the $y/z$ plane. More generally, the dimension of $\beta$ could be increased to account for the other rotational degree of freedom which must be treated in the full three-dimensional problem. Also, the input-space could be augmented to include the measured estimates of the subreflector and feedcone positions. By a principle of optimality for linear systems [8], the minimum-variance estimate for $\beta$ can be written in terms of the minimum-variance estimate for $\vec{u}$ as

$$\beta_{est} = \hat{Q}\hat{T}\hat{N}\vec{u}_{est}$$

The other statistical qualities are similarly transformed. Thus, with the definitions

$$\beta_o = \hat{Q}\hat{T}\hat{N}\vec{u}_o$$

$$(\sigma_\beta^o)^2 = E[(\beta - \beta_o)^2] \tag{13}$$

$$(\sigma_\beta^1)^2 = E[(\beta - \beta_{est})^2]$$

one can show the precise relationship between the state covariances (cf. Eqs. (3), (4)) and the boresight covariances as

$$(\sigma_\beta^o)^2 = (\hat{Q}\hat{T}\hat{N})R_\omega(\hat{Q}\hat{T}\hat{N})^*$$

$$(\sigma_\beta^1)^2 = (\hat{Q}\hat{T}\hat{N})P(\hat{Q}\hat{T}\hat{N})^*$$

These quantities can be identified with the outputs of the block diagram in Fig. 6. Thus, the quantities $\beta$, $\beta_o$, and $\beta_{est}$ respectively represent the true boresight, the modeled boresight, and the estimated boresight. The expected boresight errors before and after measurements are respectively given by $\sigma_\beta^o$ and $\sigma_\beta^1$. To these one can add a fourth boresight value

$$\tilde{\beta}_{est} = \beta_o + \hat{W}\hat{T}_{fit}\hat{N}_{fit}(\vec{y} - H\vec{u}_o)$$

Here $\beta_o$, $\vec{y}$, $\vec{u}_o$, and $H$ are as previously given, the matrix $\hat{N}_{fit}$ gives the normal projection at the observed points only, and the matrix $\hat{T}_{fit}$ is the pseudo-inverse (cf. Eq. (8)) which carries out the parabolic fit with respect to the values at the observed points only. The quantity $\tilde{\beta}_{est}$ represent the boresight estimate which is obtainable by purely geometrical analysis. In correspondence to Eq. (13), one also has an expression for the covariance:

$$\begin{aligned}(\tilde{\sigma}_\beta^1)^2 &= E[(\tilde{\beta}_{est} - \beta)^2] \\ &= (\sigma_\omega)^2 (\hat{Q}\hat{T}\hat{N})R_\omega (\hat{Q}\hat{T}\hat{N})^* \\ &\quad + (\sigma_\omega)^2 (\hat{Q}\hat{T}_{fit}\hat{N}_{fit})R_\omega (\hat{Q}\hat{T}_{fit}\hat{N}_{fit})^* \\ &\quad + (\sigma_\eta)^2 (\hat{Q}\hat{T}_{fit}\hat{N}_{fit})(\hat{Q}\hat{T}_{fit}\hat{N}_{fit})^* \\ &\quad - (\sigma_\omega)^2 (\hat{Q}\hat{T}\hat{N})R_\omega (\hat{Q}\hat{T}_{fit}\hat{N}_{fit})^* \\ &\quad - (\sigma_\omega)^2 (\hat{Q}\hat{T}_{fit}\hat{N}_{fit})R_\omega (\hat{Q}\hat{T}\hat{N})^*\end{aligned}$$

The simulations focused on the covariance analysis of the estimates. Thus, given the expected boresight error before measurements ($\sigma_\beta^o$), the number and placement of targets where measurements are taken ($H$), and the accuracy of the measurements ($\sigma_\eta$), one can calculate the expected boresight error of the estimates ($\sigma_\beta^1$, $\tilde{\sigma}_\beta^1$). For the results presented in Fig. 8, the following specifications were made. First, the model error parameter $\sigma_\omega$ was chosen so that the expected error before measurements $\sigma_\beta^o$ would be 10 millidegrees. The observation error parameter $\sigma_\eta$ was taken as 50 micrometers, a value consistent with the capability of the SHAPES system [3]. The only additional specifications required are the number and placement of targets where the displacement values are measured. Thus, in Fig. 8 the quantities $\sigma_\beta^1(j)$ and $\tilde{\sigma}_\beta^1(j)$, where $j$ is an even number, refer to the expected boresight errors with $j/2$ optimally located targets on each of the two ribs in the reduced-order antenna model. Here the optimization was carried out by evaluating all possible distinct target locations and choosing the set which gave the lowest values for the expected boresight error.

Thus, with a total of six optimally placed measurement points the structural-optical estimator achieves a ten-to-one reduction in the expected error of the estimated boresight. One should note that the structurally-based estimators are superior to the purely geometrical estimators, but they are not substantially better. This observation may be interpreted as being supportive of compensator designs based on real-time optical measurements. That is, the sophistication of the underlying estimator and the fidelity of the model may not be too important so long as measurements are available. The simulation results presented in Fig. 8 are the main quantitative outcome of this work; they demonstrate that under nominal uncertainty conditions a ten-to-one reduction in the boresight error can be achieved by integrating structural models, geometrical fitting analysis, and a real-time optical measurement system. Even though the underlying structural finite-element model may have a large dimension, the real-time computational requirements involve only matrix and vector operations where the relevant dimensions are determined by the number of measurements taken.

The results of a test case derived from the gravity model at horizon (elevation angle equals zero) are given in Fig. 9. To test the estimator's ability to recover the boresight from the measurement values only, the modeled gravitational boresight before measurements was taken to be zero ($\beta_o = 0$). For this trial the deflection was scaled to correspond to a 10-millidegree offset in the boresight, and the measurement locations were evenly spaced on each of the two ribs in the model. (The tips of the ribs were always included as measurement locations.) The measurement error was taken to be zero ($\sigma_\eta = 0$). Thus, $\beta_{est}(j)$ and $\beta_{est}(j)$ are the estimated boresight offsets with $j$ evenly spaced measurement locations.

This may be thought of as a worst-case scenario for the structurally-based estimator since the deflection is spatially biased (i.e., distorted in a preferred direction), and the estimators were designed to perform best with all distortion directions equally likely [6], [7]. Nevertheless, a ten-to-one reduction in the error is achieved. Again the geometrical estimators perform well with no structural information incorporated into the design.

Since the simple geometrical fit recovered the spatially biased component so well, this suggests that the two designs might be used in combination. First a simple geometrical fit can be performed to recover the spatially biased component, then a version of the structural-optical estimator can be implemented to obtain a finer resolution about this set point.

While additional simulations with the full three-dimensional model will be necessary to advance the design process, it is

already possible to estimate the number of measurements required to achieve a ten-to-one reduction in the pointing uncertainty. For example, two adequately resolved cross-sections would determine all the relevant parameters of a three-dimensional parabola of revolution (paraboloid). This would lead to a requirement of twelve measurements (six per cross-section). Another proposed baseline would require eighteen targets to similarly cover three cross-sections. This last design is motivated by the observation of three cross-sectional nodal lines on the main reflector of some DSN antennas; these nodal lines apparently lie on or near the best-fit paraboloid derived from the gravitational models (see, for example, [13] ).

In Fig. 10 the key locations on the antenna for the measurement system are noted. The proposed design would include approximately three SHAPES sensor heads mounted on the quadripod near the subreflector. These sensor heads would return range measurements from the targets located on the main reflector, and triangulation methods would be used to recover the displacement values relative to the sensor heads. The connection from the sensor heads to the reference plane would be made by taking additional range measurements at targets located near the origin of the reference coordinate system (base of feedcone). Calculated error estimates indicate that an additional angle-measuring camera (CCD array) at the base of the feedcone would adequately measure the angular displacement of the subreflector and the sensor heads from their nominal positions.

## IV. Conclusions

The concept proposed and analyzed in this article combines a real-time measurement system, a structural estimator, and a parabolic fitting algorithm to determine DSN antenna pointing offsets resulting from unmodeled structural distortions. This pointing offset data can be used to generate real-time command biases to correct for pointing errors. Simulations with a reduced-order antenna finite-element model have demonstrated that a ten-to-one reduction in boresight uncertainty can be achieved. The concept requires optical measurements of the displacements of selected points on the primary and secondary reflectors relative to some reference coordinate system at the base of the feedcone.

This work represents one method of improving the pointing capabilities of DSN antennas by using the techniques of the spatially random analysis of static systems. As illustrated in Fig. 11, this approach is suitable for investigating many aspects of antenna analysis related to surface deformations. While this work mainly concerns the justification of algorithms which estimate the structural boresight of an antenna, other relevant problems concerning the analysis of rms surface errors and the synthesis of antenna radiation patterns also can be studied in this framework.

## Acknowledgments

The author is indebted to C.-T. Chian for his essential contributions to the finite-element simulations. The author is also grateful to R. Levy and J. Cucchissi for many interesting discussions on the subject of this work.

## References

[1] M. D. Nelson, J. R. Schroeder, and E. F. Tubbs, "Optical Links in the Angle-Data Assembly of the 70-meter Antennas," *TDA Progress Report 42-92*, vol. October–December 1987, Jet Propulsion Laboratory, Pasadena, California, pp. 154–165, February 15, 1988.

[2] J. McLauchlan, W. Goss, and E. Tubbs, "SHAPES: A Spatial, High Accuracy, Position Encoding Sensor for Space System Control Applications," *American Astronautical Society*, Publication 82-032, January 20, 1983.

[3] N. Nerheim, "Effect of Atmospheric Turbulence on Precision Optical Measurements Used for Antenna Pointing Compensation," *TDA Progress Report 42-97*, Jet Propulsion Laboratory, Pasadena, California, this issue.

[4] L. L. Schumacher and H. C. Vivian, "Antenna Pointing Compensation Based on Precision Optical Measurement Techniques," *TDA Progress Report 42-94*, vol. April–June 1988, Jet Propulsion Laboratory, Pasadena, California, pp. 135–144, August 15, 1988.

[5] R. Levy, "Optimization of Antenna Structure Design," *Eighth Conference on Electronic Computation*, Houston, Texas, February 1983.

[6] G. Rodriguez and R. E. Scheid, "Modeling, Estimation and Identification Methods for Static Shape Control of Flexible Structures," *AAS/AIAA Astrodynamics Specialists Conference*, Vail, Colorado, August 1985.

[7] G. Rodriguez and R. E. Scheid, "An Integrated Approach to Modeling, Identification, Estimation and Control for Static Distributed Systems," *Proceedings of the Fourth IFAC Symposium on the Control of Distributed Parameter Systems*, Los Angeles, California, June 1987.

[8] A. E. Bryson and Y.-C. Ho, *Applied Optimal Control*, Washington, D.C.: Hemisphere Publishing Company, 1975.

[9] G. Rodriguez and R. E. Scheid, "Kalman-Like Estimation for Static Distributed Systems: Antenna Shape from Radiation Measurements," *Proceedings of the Fifth VPI & SU/AIAA Symposium on Dynamics and Control of Large Structures*, Blacksburg, Virginia, June 1985.

[10] M. S. Katow, *Antenna Structures: Evaluation of Reflector Surface Distortions*, JPL Technical Report 32-1526, vol. 1, Jet Propulsion Laboratory, Pasadena, California, pp. 76–80, February 15, 1971.

[11] M. S. Katow and L. W. Schmele, "Antenna Structures: Evolution Techniques of Reflector Distortions," in *Supporting Research and Advanced Development, Space Programs Summary 37-40*, vol. IV, Jet Propulsion Laboratory, Pasadena, California, pp. 176–184, August 31, 1966.

[12] G. H. Golub and C. F. Van Loan, *Matrix Computations*, Baltimore, Maryland: The Johns Hopkins University Press, 1983.

[13] Tracking and Data Acquisition Organization (Technical Staff), "The NASA/JPL 64-Meter-Diameter Antenna at Goldstone, California Project Report," *Technical Memorandum 33-671*, Jet Propulsion Laboratory, Pasadena, California, July 15, 1974.

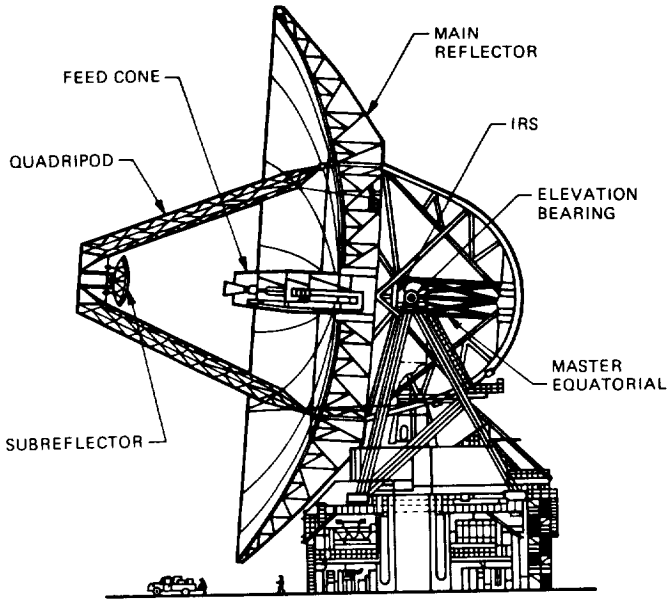


Fig. 1. 70-meter DSN antenna.

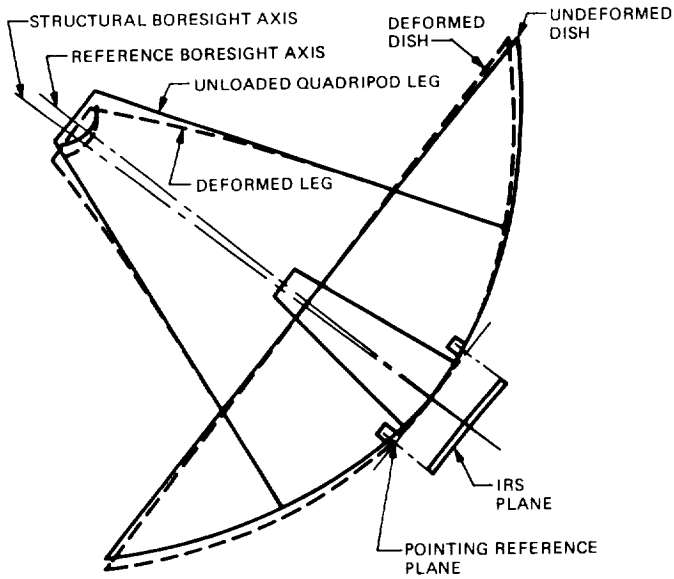


Fig. 2. Antenna deformation under loads.

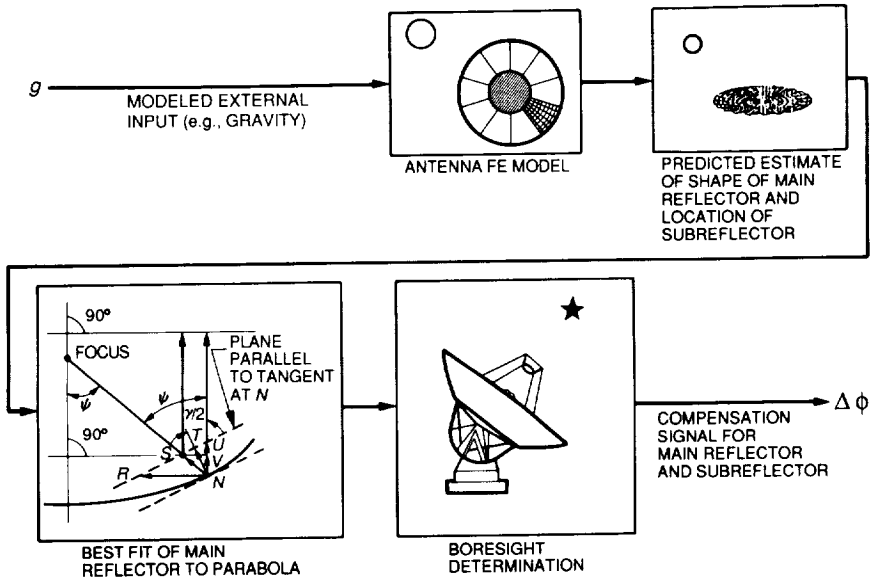


Fig. 3. Current compensator design.

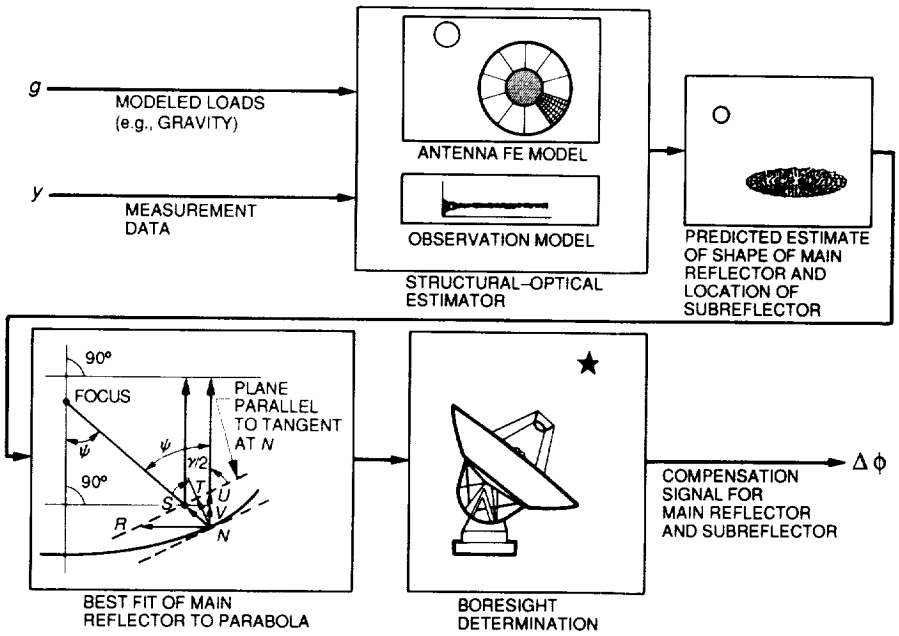


**Fig. 4. Structural-optical compensator.**

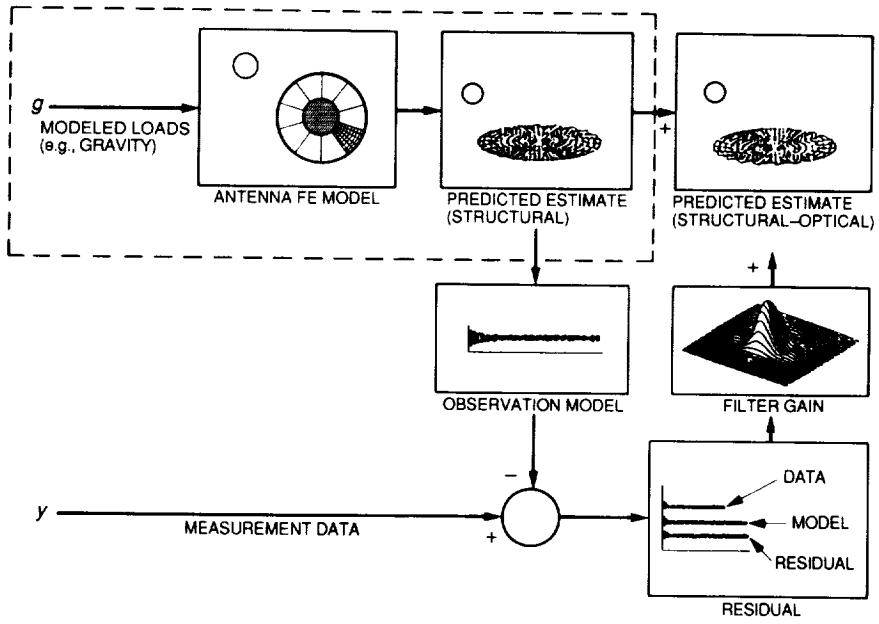


**Fig. 5. Structural-optical estimator.**

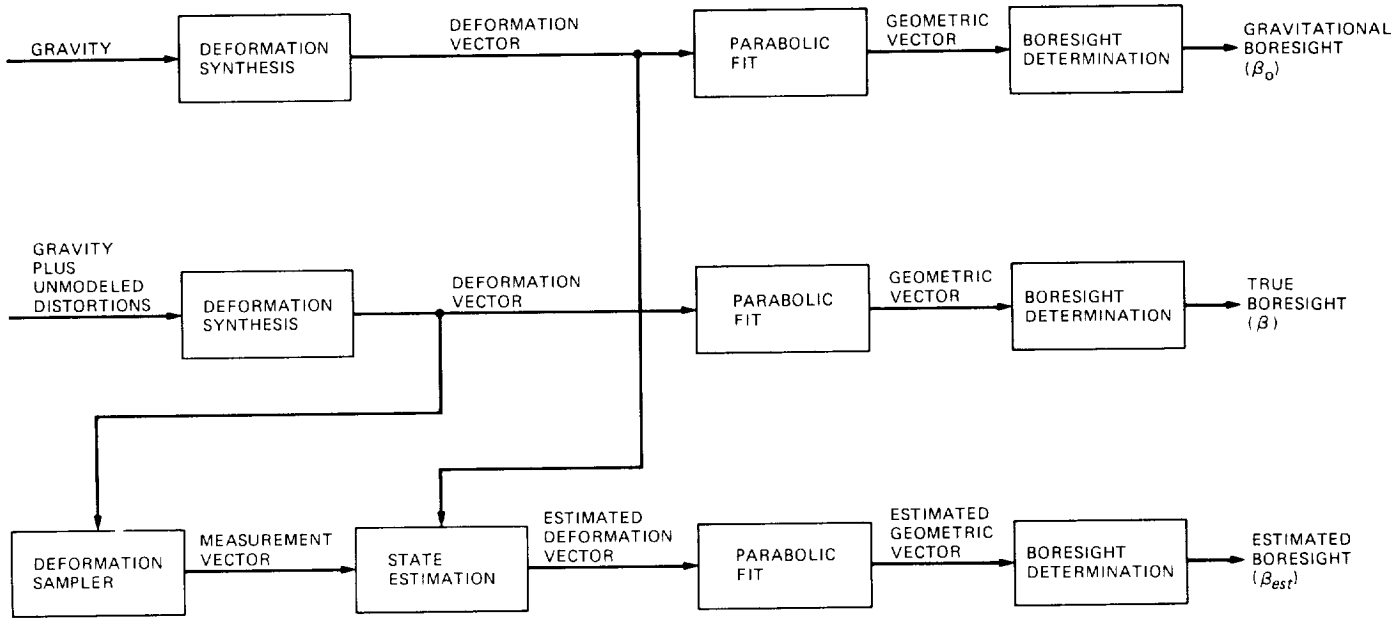


**Fig. 6. Analysis of boresight synthesis problem.**

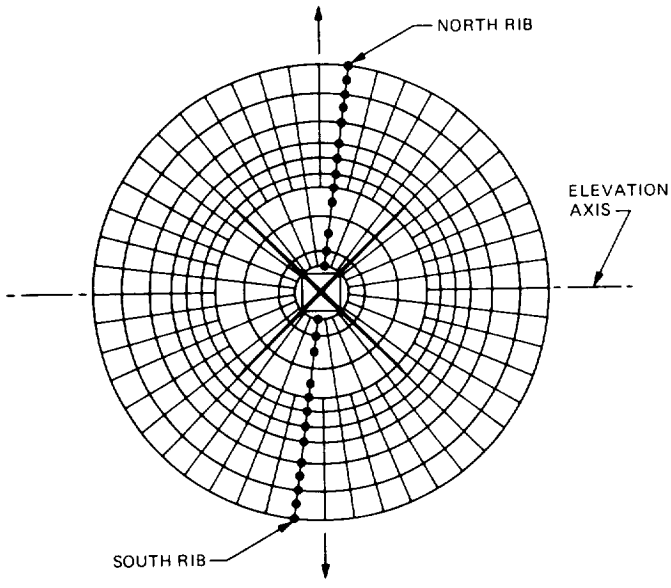


**Fig. 7. Reduced-order finite-element model of main reflector.**

| $j$ NUMBER OF OPTIMALLY LOCATED TARGETS | $\sigma_\beta^1(j)$ EXPECTED BORESIGHT ERROR, mdeg: STRUCTURAL-OPTICAL ESTIMATOR | $\tilde{\sigma}_\beta^1(j)$ EXPECTED BORESIGHT ERROR, mdeg: SIMPLE GEOMETRIC FIT |
|---|---|---|
| 2 | 1.4 | - |
| 4 | 1.1 | 1.6 |
| 6 | 0.9 | 1.3 |

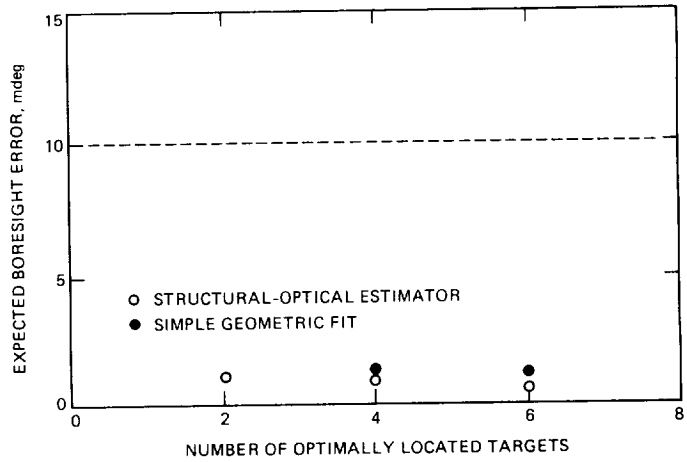


**Fig. 8. Expected boresight error ($\sigma_\beta^o$ = 10 millidegrees).**

| $i$ NUMBER OF EVENLY SPACED TARGETS | $\lvert\beta-\beta_{est}(i)\rvert$ ERROR IN BORESIGHT ESTIMATE, mdeg: STRUCTURAL-OPTICAL ESTIMATOR | $\lvert\beta-\tilde{\beta}_{est}(i)\rvert$ ERROR IN BORESIGHT ESTIMATE, mdeg: SIMPLE GEOMETRIC FIT |
|---|---|---|
| 2 | 12.8 | - |
| 4 | 7.5 | 0.8 |
| 6 | 0.2 | 0.3 |

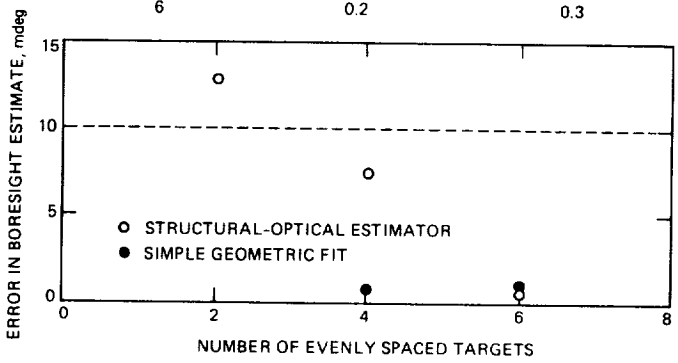


**Fig. 9. Boresight error in simulations with gravity model ($\beta$ = 10 millidegrees, $\beta_0$ = 0 millidegrees).**

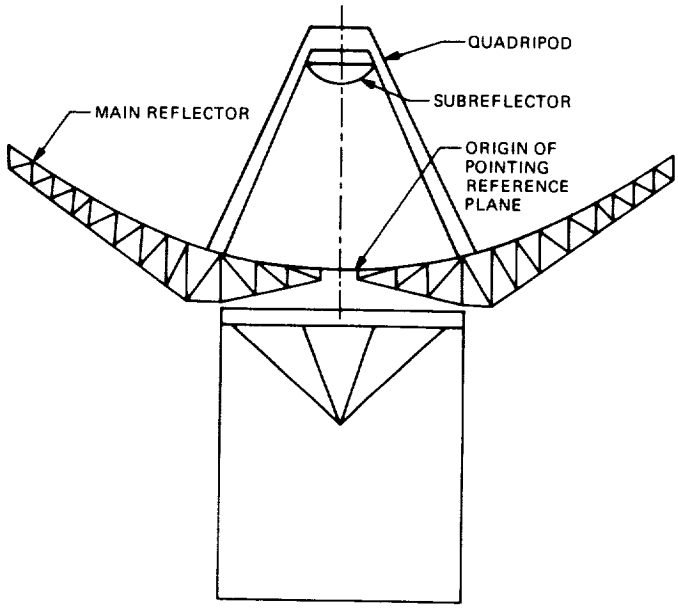


**Fig. 10. Key locations on antenna for measurement system.**

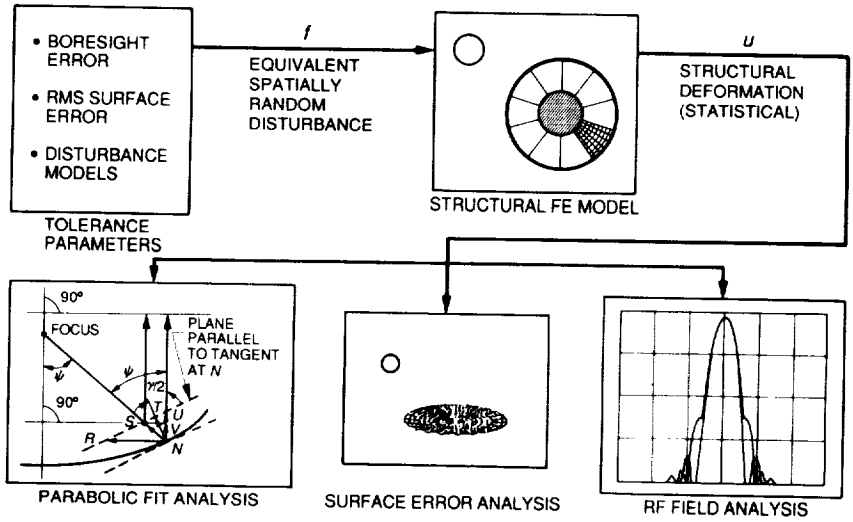


**Fig. 11. Antenna estimator design by means of spatially random disturbances.**